Beamforming in sparse, random, 3D array antennas with fluctuating element locations

Mark J. Bentum
University of Twente,
Faculty of Electrical Engineering,
Mathematics and Computer Science,
7500 AE Enschede, the Netherlands,
Email: m.j.bentum@utwente.nl

Ioan E. Lager, Sjoerd Bosma,
Wessel P. Bruinsma, Robin P. Hes
Delft University of Technology,
Faculty of Electrical Engineering,
Mathematics and Computer Science,
Mekelweg 4, 2628 CD Delft, the Netherlands,
Email: i.e.lager@tudelft.nl

***Abstract*—The impact of the fluctuations in the locations of elementary radiators on the radiation properties of three-dimensional (3D) array antennas is studied. The principal radiation features (sidelobes level, beam squint) are examined based on illustrative examples. Some atypical behaviours, that are specific to 3D arrays, are highlighted. The effect of fluctuations is demonstrated via examples concerning non-uniform arrays. This study is important for designing beamforming strategies in case of constellations of (nano) satellites for space-bound remote sensing of the Earth and the Universe.**

I. Introduction

Array antenna theory is elaborately treated in standard textbooks, e.g., [1], [2], for the case of linear and planar configurations. Surprisingly, three-dimensional (3D) array antennas (also referred to as volume or volumetric arrays) are much less covered: a general description of such arrays is given in [3, Section 10.2], some aspects concerning their synthesis are discussed in [4]–[6] and [7], [8] analyse their performance limits. Examples of practical implementations of 3D arrays are similarly scarce: the 39, 200 and 512 elements crow's nest antennas [9]–[11], with the derived design reported in [12], and the 64 element broadband volumetric array studied in [13] (with an acoustic counterpart being described in [14]).

The scarcity of 3D array antenna implementations may suggest that their specific capabilities do not weigh against the difficulty of their implementation. However, recent applications in which (more or less) randomly located radiators cooperatively resolve the bundling of radiated energy or determine the direction of arrival of an incoming (plane) wave may provide renewed incentives for the study and design of 3D arrays. One particularly interesting situation is that of constellations of (nano) satellites employed for remote sensing ends, as is the case with the Orbiting Low Frequency Antennas for Radio Astronomy (OLFAR) distributed radio telescope [15]–[17]. Such constellations may be construed as sparse, random, 3D array antennas. Beamforming in such systems may be dealt with using the instruments of the standard array antenna theory (extended such that to cope with 3D element placement). However, the fact that the satellites in the constellation have fluctuating positions, combined with limitations in the employed data aggregation methods, result in significant complications in the realisation of the relevant beamforming.

In this contribution we will study the impact of the element locations' fluctuations on the radiation properties of sparse, random, 3D array antennas. Our investigation bears similarities with the analysis in [18]. Nevertheless, while that publication dealt with (slightly) deformed planar arrays, offering solutions for calibrating out the effect of those deformations, the arrays that we study are intrinsically 3D and, moreover, the positions' perturbation that we account for is substantial.

Our account starts by discussing some basic elements of the 3D array antenna theory. We then proceed to analysing the fluctuations' impact by means of illustrative numerical examples. We round off the paper by drawing conclusions. Additionally, some background information on the OLFAR mission and on the specific beamforming strategies is included in the appendices.

II. Radiation properties of 3D antenna arrays

A. Prerequisites

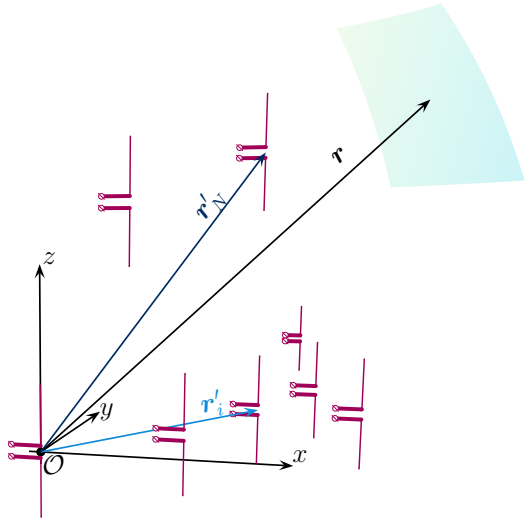

Fig. 1. 3D antenna array composed of identical elements.

The 3D array antenna under study is shown in Fig. 1. It consists of N identical elements. Although the orientation of the elements may be arbitrary, we take them, for simplicity, to be aligned. Position in the configuration is specified by

the coordinates $\{x, y, z\}$ with respect to a Cartesian reference frame with origin $\mathcal{O}$ and mutually perpendicular base vectors $\{\boldsymbol{i}_x, \boldsymbol{i}_y, \boldsymbol{i}_z\}$ of unit length each that, in this order, form a right-handed system. The position vector is $\boldsymbol{r} = x\boldsymbol{i}_x + y\boldsymbol{i}_y + z\boldsymbol{i}_z$, with $|\boldsymbol{r}| = r$ and $\boldsymbol{\xi} = \boldsymbol{r}/r$. The radiating elements' locations are denoted as $\boldsymbol{r}'_i$, $i = 1, \ldots, N$, with element 1 being located at the origin. A spherical coordinate system with the same origin and coordinates $\{\vartheta, \varphi\}$ is also considered, ϑ measuring the tilting from $\boldsymbol{i}_z$ and φ the trigonometric rotation from $\boldsymbol{i}_x$. The excitation is taken to be time-harmonic, with frequency f and angular frequency $\omega = 2\pi f$.

The array antenna radiates in free space, with electric permittivity ϵ_0, magnetic permeability μ_0 and wavespeed $c_0 = (\epsilon_0\mu_0)^{-½}$. Correspondingly, the wavenumber is $k = \omega/c_0$, the wavelength is $\lambda = c_0/f$ and the vectorial wavenumber is $\boldsymbol{k} = \boldsymbol{k}(\vartheta, \varphi) = k_x\boldsymbol{i}_x + k_y\boldsymbol{i}_y + k_z\boldsymbol{i}_z$, with

$$k_x = k\sin(\vartheta)\,\cos(\varphi) \tag{1}$$
$$k_y = k\sin(\vartheta)\,\sin(\varphi) \tag{2}$$
$$k_z = k\cos(\vartheta) \tag{3}$$

for $\vartheta \in [0, \pi]$ and $\varphi \in [0, 2\pi)$. From (1) and (2) it follows that $k_{x,y,z} \in [-k, k]$.

B. Far-field radiation of 3D antenna arrays

In line with [19], the magnitude of the far-field electric field strength radiated by an array in the observation direction $\boldsymbol{\xi}$ (given by $\{\vartheta, \varphi\}$) is expressed as

$$\begin{aligned}\boldsymbol{E}(r, \boldsymbol{\xi}) &= \frac{\mathrm{j}k}{2\pi r}\boldsymbol{A}(\boldsymbol{\xi})\sum_{i=1}^{N} w_i \exp\left[-\mathrm{j}\left(\boldsymbol{k} - \boldsymbol{k}_{\mathrm{sc}}\right)\cdot\boldsymbol{r}'_i\right] \\ &= \frac{\mathrm{j}k}{2\pi r}\boldsymbol{A}(\boldsymbol{\xi})\sum_{i=1}^{N} w_i \exp\left[-\mathrm{j}k\left(\boldsymbol{\xi} - \boldsymbol{\xi}_{\mathrm{sc}}\right)\cdot\boldsymbol{r}'_i\right]\end{aligned} \tag{4}$$

in which $\boldsymbol{A}(\boldsymbol{\xi})$ is the far-field radiation pattern of the *identical* elementary radiators, w_i are some (real) elementary weights[1], and the terms $\exp\left(\mathrm{j}\boldsymbol{k}_{\mathrm{sc}}\cdot\boldsymbol{r}'_i\right)$ $(i = 1, \ldots, N)$ represent the progressive phase shift, with $\boldsymbol{k}_{\mathrm{sc}} = \boldsymbol{k}(\boldsymbol{\xi}_{\mathrm{sc}})$ corresponding to the scanning direction $\boldsymbol{\xi}_{\mathrm{sc}}$ (given by $\{\vartheta_{\mathrm{sc}}, \varphi_{\mathrm{sc}}\}$). Note that this expression is habitually derived for planar arrays (see [1, Chapter 6], [2, Chapter 19]). Nonetheless, by observing that it is constructed using a *geometric projection* procedure, it is an easy exercise to see that it maintains its validity for the considered 3D arrays.

As usually, the array radiation properties are examined via the *directivity pattern* on a sphere S_r in the far-field region, the directivity being defined as [1, p. 39], [2, p. 602]

$$D(\boldsymbol{\xi}) = \frac{4\pi\boldsymbol{E}(r, \boldsymbol{\xi})\cdot\boldsymbol{E}^*(r, \boldsymbol{\xi})}{\int\limits_{S_r}\left[\boldsymbol{E}(r, \boldsymbol{\xi}')\cdot\boldsymbol{E}^*(r, \boldsymbol{\xi}')\right]\mathrm{d}\Omega}. \tag{5}$$

C. Principal radiation features

The principal radiation features of 3D arrays are now examined based on illustrative examples. In all cases, the elementary radiators are taken as isotropic radiators.

[1]For simplicity, in this work we take $w_i = 1$, $(i = 1, \ldots, N)$.

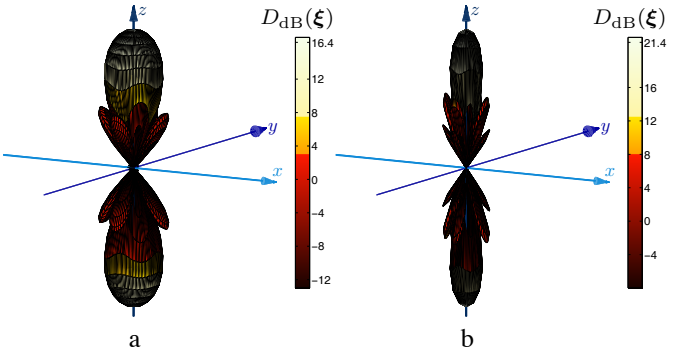

Fig. 2. Directivity patterns for $\lambda/2-$spaced array antennas consisting of (a) $5 \times 5 \times 5$ and (b) $9 \times 9 \times 5$ isotropic radiators. Broadside beam scanning.

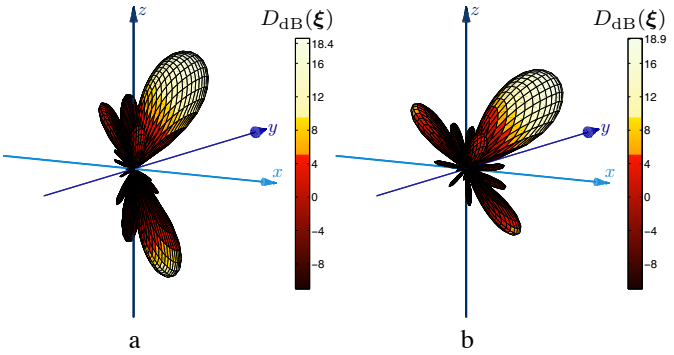

Fig. 3. Directivity patterns for a $\lambda/2-$spaced array antenna consisting of $5 \times 5 \times 5$ isotropic radiators. (a) The beam is scanned at $\{\vartheta_{\mathrm{sc}}, \varphi_{\mathrm{sc}}\} = \{30°, 0°\}$; (b) the beam is scanned at $\{\vartheta_{\mathrm{sc}}, \varphi_{\mathrm{sc}}\} = \{45°, 0°\}$.

1) Beamwidth and sidelobes level: Figure 2 shows the directivity patterns for $\lambda/2-$spaced array antennas consisting of $5 \times 5 \times 5$ and $9 \times 9 \times 5$ elements, respectively. Both cases correspond to broadside beam scanning. Like with linear and planar arrays [20], the beamwidth decreases as the array's physical dimensions increase. The radiation patterns have the same symmetry with respect to the $x\mathcal{O}y-$plane as in the case of planar arrays. As concerns the sidelobes level (SLL), the plots show that, unlike with linear and planar arrays, the relative peak SLL deviates from the well-known -13.46 dB level [1, p. 261], [3, Chapter 9]. The peak SLL variation becomes very large when the beam is scanned, as evidenced by Fig. 3. Moreover, the pattern's symmetry with respect to the $x\mathcal{O}y-$plane is also lost during scanning. Such a behaviour, that is at variance with that of linear and planar arrays, can be understood by observing that, except for broadside beam focusing, the $z-$*dependent* phase shift results, in conjunction with the arrays' layered structure, into a highly irregular interference in the sidelobes region.

2) Grating lobes: A second study concerns the onset of grating lobes. To begin with, examining Fig. 2.a shows that a $\lambda/2-$spaced array has two identical, symmetric lobes pointing at $\{0°, 0°\}$ and $\{180°, 0°\}$, respectively. This situation is similar with that encountered in case of $\lambda/2-$spaced, uniform planar arrays, the two lobes not being interpreted as grating lobes. However, the onset of grating lobes is clearly visible in Fig. 4 that shows the directivity patterns for a $\lambda-$spaced array antenna consisting of $5 \times 5 \times 5$, the beam being scanned

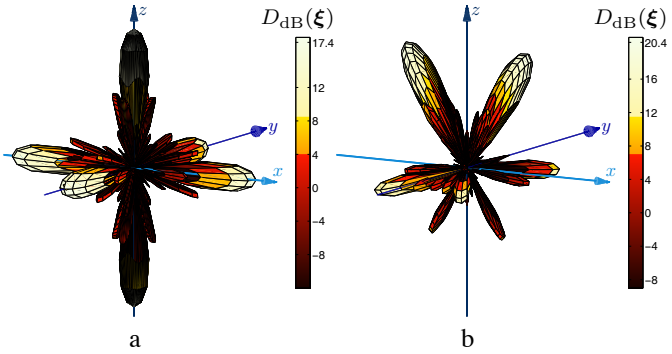

Fig. 4. Directivity patterns for a $\lambda-$spaced array antenna consisting of $5 \times 5 \times 5$ isotropic radiators. (a) Broadside beam scanning; (b) the beam is scanned at $\{\vartheta_{\mathrm{sc}}, \varphi_{\mathrm{sc}}\} = \{30°, 0°\}$.

at broadside and $\{\vartheta_{\mathrm{sc}}, \varphi_{\mathrm{sc}}\} = \{30°, 0°\}$, respectively. The symmetric distribution of grating lobes in Fig. 4.a is an effect of the array's symmetry. Interpreting the situation in Fig. 4.b is more intricate: To that end, we construe the radiated field as a superposition of end-fire radiations from planar 'slices' and apply to these planar arrays the analogy with linear arrays in [3, p. 254]. By that token, $x =$ constant 'slices' are responsible for the grating lobes in the $\{\varphi = 90° \cup \varphi = 270°\}-$plane while $y =$ constant 'slices' are responsible for the grating lobes in the $\{\varphi = 0° \cup \varphi = 180°\}-$plane. This interpretation is valid in those planes, only, the quantitative study of the directivity pattern's shape outside those planes being more intricate.

III. Impact of Fluctuations in the Array Architecture on the Radiation Properties

A. Examined configurations

As a starting point, we examine the situations of 3D array antennas consisting of 81 isotropic radiators, the projections of the elements onto the $x\mathcal{O}y-$plane forming 9×9 uniform lattices spaced at $\lambda/2$ (see Fig. 5) or at λ (see Fig. 6), respectively. These configurations are deemed representative for (admittedly, rather large) constellations of nano-satellites. The radiation properties of the 2 arrays are examined for broadside radiation and for a beam scanning at $\{\vartheta_{\mathrm{sc}}, \varphi_{\mathrm{sc}}\} = \{30°, 0°\}$. As expected, the broadside patterns are symmetric with respect to the $x\mathcal{O}y-$plane, but the symmetry is lost when the beam is scanned. The grating lobes' onset is illustrated in Fig. 6.b. Nonetheless, as a result of the spatial spreading of the elementary radiators, the 'grating lobe' in Fig. 6.c is lower than the main lobe. This behaviour is reminiscent of that of the 3D uniform arrays examined in Section II-C.

B. Location perturbation study

The elements' locations in the arrays shown in Figs. 5.a and 6.a (henceforth referred to as "original") are now perturbed according to the expression

$$\boldsymbol{r}'_{n;\mathrm{pert}} = \boldsymbol{r}'_n \, \mathcal{K} \left(\tilde{x}_n \boldsymbol{i}_x + \tilde{y}_n \boldsymbol{i}_y + \tilde{z}_n \boldsymbol{i}_z\right) \quad \text{for } n = 1, \ldots, N \quad (6)$$

with $\mathcal{K}$ being a scaling factor and $\tilde{x}_n$, $\tilde{y}_n$, $\tilde{z}_n$ being random real numbers between -1 and 1. In our experiments we take $\mathcal{K} = 10\%$. The progressive phase shifts are still those corresponding

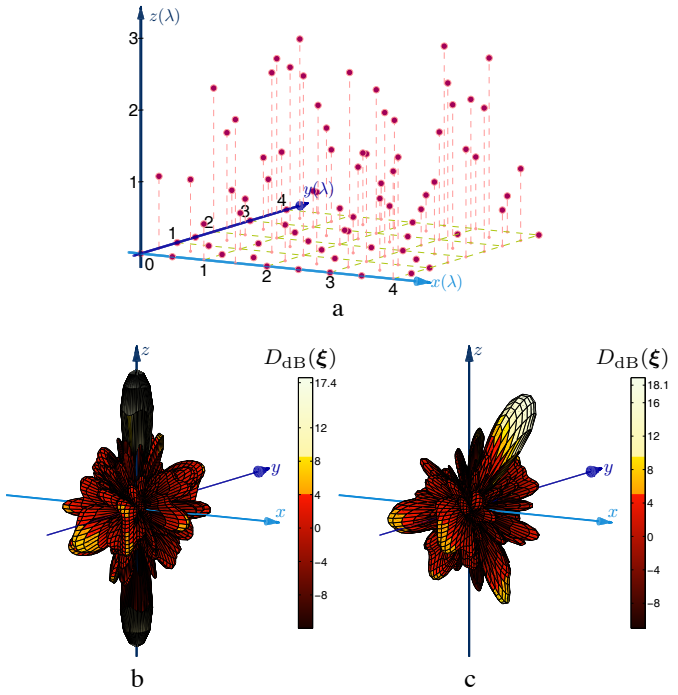

Fig. 5. Directivity patterns for an array antenna consisting of 81 isotropic radiators. The elements' projections onto the $x\mathcal{O}y-$plane form a $\lambda/2-$spaced, 9×9 uniform lattice. (a) Array configuration; (b) broadside directivity pattern; (c) directivity pattern with the beam scanned at $\{\vartheta_{\mathrm{sc}}, \varphi_{\mathrm{sc}}\} = \{30°, 0°\}$.

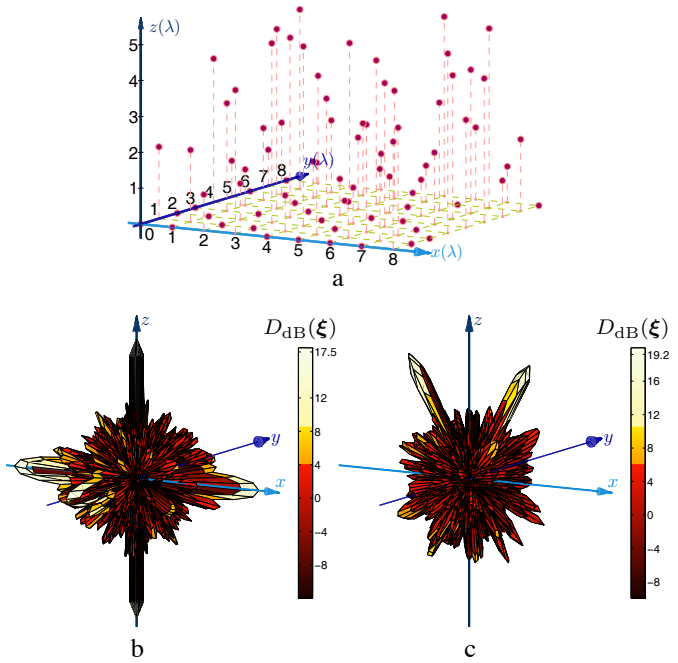

Fig. 6. Directivity patterns for an array antenna consisting of 81 isotropic radiators. The elements' projections onto the $x\mathcal{O}y-$plane form a $\lambda-$spaced, 9×9 uniform lattice. (a) Array configuration; (b) broadside directivity pattern; (c) directivity pattern with the beam scanned at $\{\vartheta_{\mathrm{sc}}, \varphi_{\mathrm{sc}}\} = \{30°, 0°\}$.

to the original locations. With these choices, (4) becomes

$$\boldsymbol{E}(r, \boldsymbol{\xi}) = \frac{\mathrm{j}k}{2\pi r} \boldsymbol{A}(\boldsymbol{\xi}) \sum_{i=1}^{N} w_i \exp\left[-\mathrm{j}k \left(\boldsymbol{\xi} \cdot \boldsymbol{r}'_{i;\mathrm{pert}} - \boldsymbol{\xi}_{\mathrm{sc}} \cdot \boldsymbol{r}'_i\right)\right]. \quad (7)$$

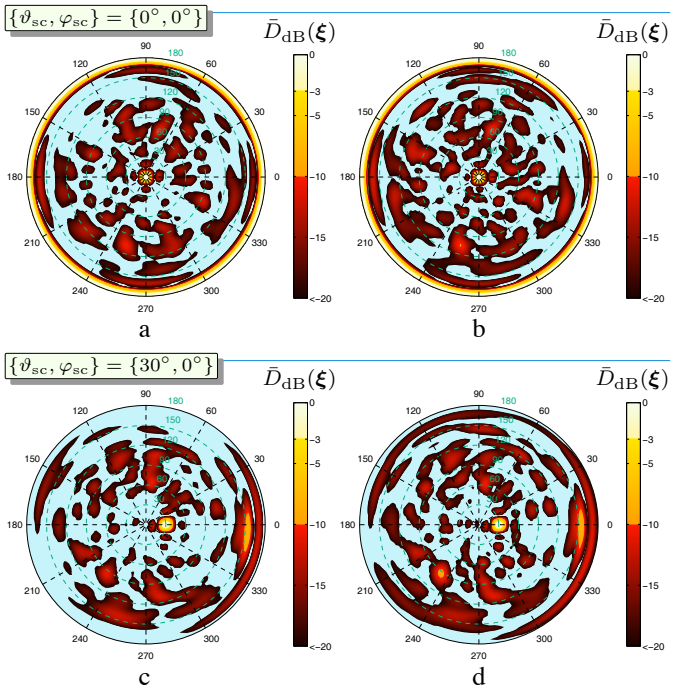

Fig. 7. Normalised directivity patterns for an array antenna consisting of 81 isotropic radiators. The *unperturbed array's* elements' projections onto the $x\mathcal{O}y-$plane form a $\lambda/2-$spaced, 9×9 uniform lattice. (a) Unperturbed array, broadside directivity pattern; (b) perturbed array, broadside directivity pattern; (c) unperturbed array, directivity pattern with the beam scanned at $\{\vartheta_{\rm sc}, \varphi_{\rm sc}\} = \{30^\circ, 0^\circ\}$; (d) perturbed array, directivity pattern with the beam scanned at $\{\vartheta_{\rm sc}, \varphi_{\rm sc}\} = \{30^\circ, 0^\circ\}$.

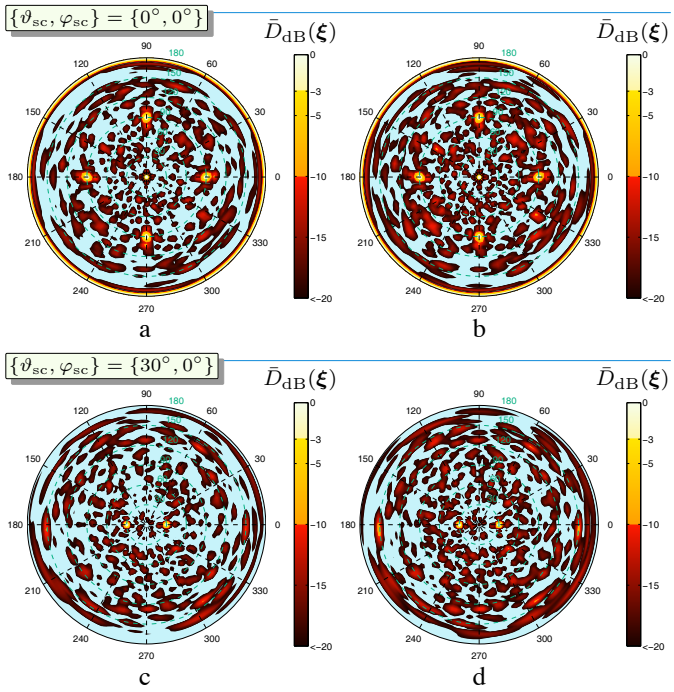

Fig. 8. Normalised directivity patterns for an array antenna consisting of 81 isotropic radiators. The *unperturbed array's* elements' projections onto the $x\mathcal{O}y-$plane form a $\lambda-$spaced, 9×9 uniform lattice. (a) Unperturbed array, broadside directivity pattern; (b) perturbed array, broadside directivity pattern; (c) unperturbed array, directivity pattern with the beam scanned at $\{\vartheta_{\rm sc}, \varphi_{\rm sc}\} = \{30^\circ, 0^\circ\}$; (d) perturbed array, directivity pattern with the beam scanned at $\{\vartheta_{\rm sc}, \varphi_{\rm sc}\} = \{30^\circ, 0^\circ\}$.

Moreover, for better highlighting the impact of the fluctuations of the locations on the resulting radiation patterns, we hereafter focus on the *normalised* directivity

$$\bar{D}_{\rm dB}(\boldsymbol{\xi}) = D_{\rm dB}(\boldsymbol{\xi}) / |D_{\rm dB}(\boldsymbol{\xi})|_{\max}. \tag{8}$$

Note that our numerical experiments have shown that, as expected, the impact of those fluctuations on the maximum directivity is extremely reduced, if any.

Hereafter, we focus on the sidelobes' distribution and level and on the squint of the main beam. The $\bar{D}_{\rm dB}(\boldsymbol{\xi})$ patterns are shown in Figs. 7 and 8 for the original and perturbed arrays.

As concerns the behaviour of the original arrays, the plots demonstrate the highly irregular distribution of sidelobes that is inherent to non-uniform array antennas (as documented in, e.g., [21], [22]). The grating lobes in the case of the $\lambda-$spaced array are also clearly visible.

When moving to the perturbed arrays, it is firstly observed that the SLL increases, with significantly more sidelobes raising above the -20dB level (especially in the case of the $\lambda-$spaced array). In order to zoom in on the SLL, Table I lists the levels of the 10 highest lobes (grating lobes including) in the case of the examined arrays. The obtained levels change, but not much, and the location of some of the relevant lobes is different. Another interesting remark is that, due to the location randomisation, some of the grating lobes in the case of the under-sampled array disappear – they change into high sidelobes, be it with levels close to 0dB. As for the fluctuations induced beam squint, from Table I it can be inferred that it is negligible.

Our analysis demonstrates that even small fluctuations of the elements' locations impact on the radiation pattern of the array of a type that is representative for a constellation of nano-satellites. The most pronounced effect is on the SLL. Depending of the application at hand, the increase in the SLL may lead to (significant) degradation of the system performance and measures to compensate for the perturbation may have to be called upon, with [18] offering possible guidelines.

IV. Conclusions

The impact of the fluctuations in the locations of elementary radiators on the radiation properties of three-dimensional (3D) array antennas was studied. The principal radiation features, e.g., beamwidth, sidelobes level (SLL), and the effect of the element locations' fluctuations on these metrics were examined based on illustrative examples. Our study has shown that even small fluctuations result in an increase of the sidelobes, although the peak SLL does not change significantly. Together with the pertaining investigation instruments, this study is expedient for, among others, designing beamforming strategies in case of constellations of (nano) satellites for space-bound remote sensing of the Earth and the Universe.

Appendix

A. The OLFAR mission

One of the last unexplored frequency ranges in radio astronomy is the frequency band below 30 MHz. New interesting astronomical science drivers for very low frequency

TABLE I. COMPARISON BETWEEN THE LEVELS AND THE POSITIONING OF THE FIRST 5 HIGHEST LOBES IN THE CASE OF THE ARRAYS IN FIGS. 5.A AND 6.A (ORIGINAL) AND THEIR BY 10% PERTURBED COUNTERPARTS. THE HIGHLIGHTED VALUES CORRESPOND TO THE MAIN LOBES.

Array: $\lambda/2-$spaced, 9×9 uniform lattice								Array: $\lambda-$spaced, 9×9 uniform lattice							
$\{\vartheta_{sc}, \varphi_{sc}\} = \{0^\circ, 0^\circ\}$				$\{\vartheta_{sc}, \varphi_{sc}\} = \{30^\circ, 0^\circ\}$				$\{\vartheta_{sc}, \varphi_{sc}\} = \{0^\circ, 0^\circ\}$				$\{\vartheta_{sc}, \varphi_{sc}\} = \{30^\circ, 0^\circ\}$			
Original		Perturbed		Original		Perturbed		Original		Perturbed		Original		Perturbed	
0	$\{0^\circ, 0^\circ\}$	**0**	$\{0.5^\circ, 179.5^\circ\}$	**0**	$\{30^\circ, 179.5^\circ\}$	**0**	$\{30^\circ, 179.5^\circ\}$	**0**	$\{0^\circ, 0^\circ\}$	**0**	$\{0.5^\circ, 179.5^\circ\}$	**0**	$\{30^\circ, 179.5^\circ\}$	**0**	$\{30^\circ, 179.5^\circ\}$
0	$\{180^\circ, 180.5^\circ\}$	0	$\{179.5^\circ, 359.5^\circ\}$	-7.5	$\{154^\circ, 175.5^\circ\}$	-7.7	$\{155^\circ, 178.5^\circ\}$	0	$\{90^\circ, 269.5^\circ\}$	0	$\{179.5^\circ, 359.5^\circ\}$	0	$\{30^\circ, 359.5^\circ\}$	-0.2	$\{29.5^\circ, 0.5^\circ\}$
-10.2	$\{72.5^\circ, 253.5^\circ\}$	-9.7	$\{73.5^\circ, 301^\circ\}$	-10.3	$\{63.5^\circ, 262^\circ\}$	-8.9	$\{93^\circ, 52^\circ\}$	0	$\{90^\circ, 179.5^\circ\}$	0	$\{90^\circ, 227.5^\circ\}$	-9	$\{151.5^\circ, 2^\circ\}$	-7.9	$\{151.5^\circ, 2.5^\circ\}$
-10.2	$\{107.5^\circ, 73.5^\circ\}$	-9.7	$\{106.5^\circ, 121^\circ\}$	-10.8	$\{94^\circ, 50.5^\circ\}$	-10.3	$\{62.5^\circ, 261^\circ\}$	0	$\{90^\circ, 89.5^\circ\}$	0	$\{90^\circ, 47.5^\circ\}$	-9.2	$\{141.5^\circ, 235^\circ\}$	-7.9	$\{150.5^\circ, 177.5^\circ\}$
-11.4	$\{87^\circ, 336.5^\circ\}$	-11.3	$\{19.5^\circ, 227^\circ\}$	-11.4	$\{109.5^\circ, 100^\circ\}$	-10.9	$\{171.5^\circ, 167.5^\circ\}$	0	$\{90^\circ, 359.5^\circ\}$	-0.2	$\{90^\circ, 317.5^\circ\}$	-9.2	$\{143^\circ, 126^\circ\}$	-9	$\{143^\circ, 126.5^\circ\}$
-11.4	$\{93^\circ, 156.5^\circ\}$	-11.3	$\{160.5^\circ, 47^\circ\}$	-11.5	$\{105.5^\circ, 262^\circ\}$	-11.1	$\{109^\circ, 101^\circ\}$	0	$\{180^\circ, 180^\circ\}$	-0.2	$\{90^\circ, 137.5^\circ\}$	-9.5	$\{150^\circ, 177^\circ\}$	-9.1	$\{141^\circ, 236^\circ\}$
-11.9	$\{19^\circ, 182^\circ\}$	-11.3	$\{90^\circ, 25^\circ\}$	-11.5	$\{9.5^\circ, 170.5^\circ\}$	-11.4	$\{88.5^\circ, 95.5^\circ\}$	-8.5	$\{77^\circ, 268.5^\circ\}$	-8.7	$\{77^\circ, 13.5^\circ\}$	-9.6	$\{57^\circ, 140.5^\circ\}$	-9.2	$\{127^\circ, 91.5^\circ\}$
-11.9	$\{161^\circ, 2^\circ\}$	-11.3	$\{90^\circ, 205^\circ\}$	-11.6	$\{170.5^\circ, 169.5^\circ\}$	-11.4	$\{97.5^\circ, 325.5^\circ\}$	-8.5	$\{103^\circ, 88.5^\circ\}$	-8.7	$\{103^\circ, 193.5^\circ\}$	-10.2	$\{122.5^\circ, 142.5^\circ\}$	-9.2	$\{56.5^\circ, 140.5^\circ\}$
-12.5	$\{80^\circ, 108^\circ\}$	-11.6	$\{44^\circ, 29^\circ\}$	-11.9	$\{143.5^\circ, 72^\circ\}$	-11.8	$\{58^\circ, 96.5^\circ\}$	-8.5	$\{77^\circ, 0.5^\circ\}$	-9.1	$\{77^\circ, 316^\circ\}$	-10.3	$\{122.5^\circ, 216^\circ\}$	-10.1	$\{141.5^\circ, 298.5^\circ\}$
-12.5	$\{100^\circ, 288^\circ\}$	-11.6	$\{136^\circ, 209^\circ\}$	-12.5	$\{106^\circ, 291^\circ\}$	-11.8	$\{123^\circ, 238^\circ\}$	-8.5	$\{103^\circ, 180.5^\circ\}$	-9.1	$\{103^\circ, 136^\circ\}$	-10.8	$\{127^\circ, 91^\circ\}$	-10.3	$\{97.5^\circ, 301.5^\circ\}$

radio astronomy have emerged, ranging from studies of the astronomical dark ages, the epoch of re-ionisation, exoplanets, to ultra-high energy cosmic rays. However, astronomical observations with Earth-bound radio telescopes at very low frequencies are hampered by the ionospheric plasma, which scatters impinging celestial radio waves. Sometimes the ionosphere is even opaque for radio waves. Although the ionosphere is transparent at frequencies above roughly 10 MHz, Earth-bound radio astronomy is affected by the short-term phase fluctuations of the received celestial radio waves. An additional factor which limits the sensitivity of Earth-bound radio telescopes at frequencies in the band below 30 MHz, is the Radio Frequency Interference (RFI) as a result of the world-wide occurrence of very strong transmitter signals in that band. A radio telescope in space would not be hampered by the Earth's ionosphere and RFI.

For this reason the Orbiting Low-Frequency Antennas for Radio Astronomy (OLFAR) project aims to develop a space-based radio telescope, consisting of 50 or more nano-satellites in a location far away from Earth. These satellites will be flying in a swarm approximately 100 km in diameter to synthesise a large radio aperture.

B. OLFAR data: acquiring and processing

Each of the satellites in the OLFAR swarm will capture the long wavelenght signal using three orthogonal detectors with good sensitivity in as large a field of view (FoV) as possible, as the direction of incidence of the incoming EM waves is not known a priori. This data is then employed for imaging and beamforming [17].

REFERENCES

[1] C. A. Balanis, *Antenna Theory: Analysis and Design*, 2nd ed., New York: John Wiley & Sons Inc., 1997.

[2] S. J. Orfanidis, *Electromagnetic Waves and Antennas*, [Online]. Available: www.ece.rutgers.edu/ orfanidi/ewa.

[3] H. J. Visser, *Array and Phased Array Antenna Basics*, Hoboken, NJ: John Wiley & Sons Inc., 2005.

[4] R. Voles, "Spherical shell and volume arrays," *IEE Proc-H*, vol. 142, no. 6, pp. 498–500, Dec. 1995.

[5] J. M. Rigelsford and A. Tennant, "A synthetic acoustic volumetric array," in *Proc. SAM 2006*, Waltham, MA, Jul. 2006, pp. 313–314.

[6] J. M. Rigelsford and A. Tennant, "Sidelobe reduction in a random spherical volumetric array using frequency diversity," *Applied Acoustics*, vol. 74, no. 6, pp. 865-869, Jun. 2013.

[7] D. T. Vu, A. Renaux, R. Boyer, and S. Marcos, "Performance analysis of 2D and 3D antenna arrays for source localization," in *Proc. 1^{th} EUSIPCO-2010*, Aalborg, Denmark, Aug. 2010, pp. 661–665.

[8] D. T. Vu, A. Renaux, R. Boyer, and S. Marcos, "A Cramr Rao bounds based analysis of 3D antenna array geometries made from ULA branches," *Multidim Syst Sign Process*, vol. 24, no. 1, pp. 121-155, Mar. 2013.

[9] H. Wilden, "Crow's-nest antenna," *Electron. Lett.* vol. 16, no. 7, pp. 256–257, Mar. 1980.

[10] H. Wilden and J. Ender, "The crow's-nest antenna - special aspects and results," in *Proc. 17^{th} EuMC*, Rome, Italy, Sep. 1987, pp. 509–514.

[11] H. Wilden and J. Ender, "The crow's nest antenna – experimental results," in *Rec. IEEE 1990 International Radar Conference*, Arlington, VA, May 1990, pp. 280–285.

[12] J. A. Scholz, "Volumetric phased array antenna system," US Patent 6,636,177 B1, Oct. 21, 2003.

[13] A. Tennant, A. F. Fray, D. B. Adamson, and M. W. Shelley, "Beam scanning characteristics of 64 element broadband volumetric array," *Electron. Lett.* vol. 33, no. 24, pp. 2001–2002, Nov. 1997.

[14] J. M. Rigelsford and A. Tennant, "A 64 element acoustic volumetric array," *Applied Acoustics*, vol. 61, no. 4, pp. 469–475, Dec. 2000.

[15] M. J. Bentum, C. J. M. Verhoeven, A. J. Boonstra, A. J. van der Veen and E. K. A. Gill, "A Novel Astronomical Application for Formation Flying Small Satellites," in *Proc. of the 60^{th} International Astronautical Congress*, Daejeon, Republic of Korea, Oct. 2009.

[16] R. T. Rajan, S. Engelen, M. J. Bentum, and C. J. M. Verhoeven, "The Orbiting Low Frequency Antenna Array," in *Proc. of the IEEE Aerospace*, Big Sky, Montana, USA, March. 2011.

[17] P. K. A. van Vugt, A. Meijerink and M. J. Bentum, "Calibration Approach of the OLFAR Space Based Radio Telescope," in *Proc. of the 65^{th} International Astronautical Congress*, Toronto, Canada, Sep. 2014.

[18] G. Lesueur, D. Caer, T. Merlet, and P. Granger, "Active compensation techniques for deformable phased array antenna," in *Proc. 3^{rd} EuCAP*, Berlin, Germany, Mar. 2009, pp. 1578–1581.

[19] I. E. Lager and M. Simeoni, "Radiation properties of non-uniform array antennas," in *Proc. 42^{nd} EuMC*, Amsterdam, the Netherlands, Oct.-Nov. 2012, pp. 502–505.

[20] C. I. Coman, I. E. Lager, and L. P. Ligthart, "Design considerations in sparse array antennas," in *Proc. 3^{rd} EuRAD*, Manchester, UK, Sep. 2006, pp. 72–75.

[21] M. C. Viganò, G. Toso, G. Caille, C. Mangenot and I. E. Lager, "Sunflower array antenna with adjustable density taper," *Int. Journal of Antennas and Propagation, Hindawi Publ. Corp.*, vol. 2009, Article ID 624035.

[22] M. C. Viganò, G. Toso, P. Angeletti, I. E. Lager, A. Yarovoy, and D. Caratelli, "Sparse antenna array for Earth-coverage satellite applications," in *Proc. 4^{rd} EuCAP*, Barcelona, Spain, Apr. 2010.